

# Spectral energy transfer and generation of turbulent structures in toroidal plasma

H. Xia<sup>a)</sup> and M. G. Shats

*Plasma Research Laboratory, Research School of Physical Sciences and Engineering,  
Australian National University, Canberra ACT 0200, Australia*

(Received 31 July 2003; accepted 3 November 2003)

Nonlinear energy cascades in turbulent spectra are studied in the H-1 toroidal heliac [S. M. Hamberger *et al.*, *Fusion Technol.* **17**, 123 (1990)] using the spectral energy transfer estimation and the amplitude correlation technique. An inverse energy cascade of the spectral energy from the unstable range is shown to be responsible for the generation of the large-scale coherent structures dominating turbulence spectra. Among such structures are zonal flows which are also found to be generated via the inverse cascade. The generation of zonal flows is correlated with the increased strength in the nonlinear energy transfer. The onset of the strongly sheared radial electric field across the low-high (L-H) transition dramatically changes the energy transfer in the spectra and the spectral power of the fluctuations. © 2004 American Institute of Physics.  
[DOI: 10.1063/1.1637607]

## I. INTRODUCTION

Turbulence is believed to be the reason for anomalously high radial particle and heat transport in magnetically confined plasma. Since the anomalous transport limits the efficiency of the energy confinement in fusion experiments, it is very important to understand and control turbulence.

The role played by long-living structures in plasma turbulence has become an important issue in the last decades.<sup>1</sup> Vortex-like structures have been observed under different plasma conditions, both experimentally<sup>2–6</sup> and in numerical simulations.<sup>7–9</sup> Interactions between flows and turbulent structures is the central point of the turbulence self-regulation concept<sup>10</sup> that is being developed with regard to magnetized plasmas. Both mean (time average) and the time-varying shear flows can be generated by turbulence, and both affect their parent waves and modify the turbulent transport.<sup>11</sup> Time-varying shear flows, or zonal flows, affect their parent fluctuations and the turbulent-driven fluxes through the mechanism of random shearing.<sup>12</sup> Recently the effect of zonal flows on the fluctuation-driven particle flux has been experimentally shown to be dramatic in toroidal plasma.<sup>13</sup> It is very important to understand the formation, propagation and suppression of large-scale fluctuation structures, including zonal flows.

Plasma turbulence is often characterized by broad fluctuation spectra whose maxima are observed at the longest measured scales. Since waves are usually unstable in a limited spectral range, a nonlinear mechanism of the wave-wave interaction in the plasma is necessary to explain turbulent spectra. Such a nonlinear mechanism, namely three-wave interactions which lead to the energy cascade, has been shown to be important in the two-dimensional turbulence<sup>14</sup> and in the magnetized plasma.<sup>15</sup> In some conditions the “inverse cascade,” or the nonlinear spectral energy transfer to-

wards lower wave numbers has been predicted. According to theory, the spectral energy can condensate due to the inverse cascade in large coherent structures, such as vortex structures (for review see Ref. 1) and zonal flows.<sup>16</sup> However, very few experimental results are available that verify the role of the inverse cascade in the generation of broadband spectra and structures. Estimating the nonlinear energy transfer in the fluctuation spectrum is one of the main problems.

A higher-order spectrum analysis has long been used in the turbulence studies to characterize nonlinear interactions between fluctuations.<sup>17</sup> Bispectra, bicoherence, and summed bicoherence have been used to measure the strength of the three-wave interactions. In order to make a quantitative estimation of the energy cascade between waves in a turbulent plasma, a technique of power transfer function estimation (PTF), which uses the higher-order spectral analysis, has been developed by Ritz *et al.*<sup>18,19</sup> and has been applied to the data from the Texas Experimental Tokamak (TEXT) edge turbulence. This model is suitable for studying the spectral dynamics in single-field turbulence, such as neutral fluid turbulence, or the Hasegawa-Mima turbulence in plasma.<sup>20</sup> Later an extended version of this technique is proposed by Kim *et al.*<sup>21</sup> and it has been applied to the Tokamak Fusion Test Reactor (TFTR) plasma core fluctuations.<sup>22</sup> In both TEXT and TFTR no strong cascade of the fluctuation power to lower wave numbers has been found. One difficulty might have been that the Hasegawa-Mima-type turbulence is not commonly observed in fusion plasma experiments.

Crossley *et al.*<sup>23</sup> have proposed the amplitude correlation technique for the nonlinear energy transfer study and have found evidence of the inverse cascade in the fluctuation spectra of the University of Manchester Institute of Science and Technology (UMIST) quadrupole. In their work the observed spectrum contains regions of growth at high frequency and damping at low frequency with the flow down the spectrum via a cascade mediated by the flute-like modes. The ampli-

<sup>a)</sup>Electronic mail: hua.xia@anu.edu.au

tude correlation technique provides a direct way of determining the direction of the energy flow. It has been pointed out, however, that dispersive wave systems without nonlinearity may possibly give rise to a nonzero amplitude correlation.<sup>24</sup> The physical meaning of the amplitude correlation needs to be verified by some other nonlinear energy flow estimation method, such as the power transfer function technique mentioned above.

The generation of spectral condensate including zonal flow through the inverse energy cascade has been predicted by early theoretical work of Hasegawa *et al.*<sup>16</sup> The first observation of the zonal flow in numerical modelling has been reported by Lin *et al.*<sup>12</sup> Zonal flows have been experimentally observed in the H-1 (Heliac-1) (Ref. 25) and in the DIII-D tokamak.<sup>26</sup> However the role of three-wave interactions in the generation of zonal flows still needs to be addressed in experiments to verify the importance of the inverse energy cascade. Recently we have reported the first experimental evidence that the inverse energy cascade correlates with the generation of large structures.<sup>27</sup>

In this paper we present detailed studies of the mechanisms of the structure generation including zonal flows and the role of energy cascades in these processes. The paper is organized as follows. Plasma conditions and turbulence description are given in Sec. II. The applicability of a single-field model to the H-1 heliac plasma turbulence is presented. Also in Sec. II we discuss two main spectral transfer analysis techniques used in the paper. Section III presents results on the energy cascades and on the turbulent structure generation.

## II. EXPERIMENTAL CONDITIONS AND DATA ANALYSIS METHODS

### A. Plasma parameters

We present the analysis of turbulence measured in the H-1 toroidal heliac.<sup>28</sup> This is a three-field period helical axis stellarator with a major radius of  $R=1$  m and mean minor plasma radius of about  $\langle a \rangle \approx 0.2$  m. The plasma parameters are as follows (see, for example Ref. 29, and references therein):  $n_e = 1 \times 10^{18} \text{ m}^{-3}$ ,  $T_e \sim 10$  eV,  $T_i \sim 40$  eV in argon at filling pressure of  $(1-4) \times 10^{-5}$  Torr and at low magnetic fields,  $B = (0.05-0.12)$  T. Such plasma is produced by  $\sim 60$  kW of the radio-frequency waves at 7 MHz. Various combinations of electric probes are used to characterize plasma parameters. Triple probes provide the information on fluctuations in the floating potential,  $V_f$ , plasma potential,  $V_p$ , and the ion saturation current,  $I_{\text{sat}}$ . Radial and poloidal electric fields and corresponding fluctuation wave numbers can be derived from the probe measurements. We analyze fluctuations in the floating potential,  $\tilde{V}_f$ , rather than the plasma potential to achieve the best signal to noise ratio to which the higher order spectral analysis is very sensitive. The amplitude and the phase spectra of the electron temperature fluctuations in our conditions have been found to be identical to those in the floating potential. Therefore this simplification does not affect our results.

Strong fluctuations in the electron density ( $\tilde{n}_e/\bar{n}_e \sim 0.25$ ) and in the electrostatic potential are observed in the

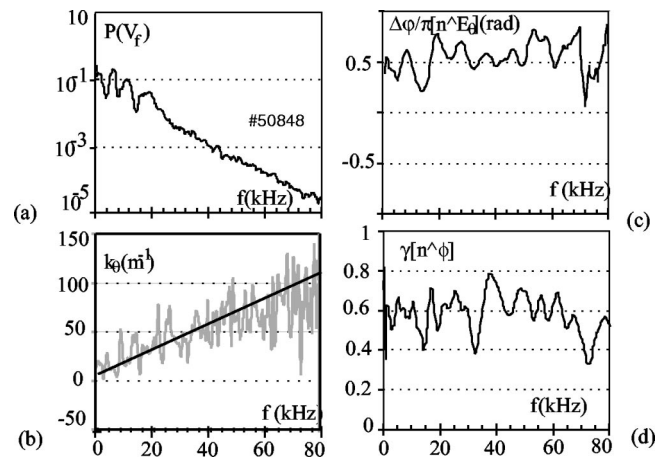


FIG. 1. (a) Power spectrum of the fluctuations in the floating potentials,  $\tilde{V}_f$ , at  $r/a=0.5$ ,  $B=0.052$  T,  $P_{\text{rf}}=55$  kW; (b) the measured poloidal wave number spectrum  $k_\theta(f)$  (gray line) with the linear fit (black line). Spectra of (c) the phase shift between fluctuations in the electron density,  $\tilde{n}_e$  and poloidal electric field,  $\tilde{E}_\theta$ ; and (d) the coherence between fluctuations in the electron density,  $\tilde{n}_e$  and the floating potential,  $\tilde{V}_f$ .

H-1 plasma at low magnetic fields ( $B < 0.1$  T).<sup>30</sup> An identification of these fluctuations is not certain but we have found several signatures of the resistive pressure-gradient-driven instability.<sup>30</sup> A frequency power spectrum of the  $\tilde{V}_f$  fluctuations in the low confinement mode<sup>30</sup> is presented in Fig. 1(a). The spectrum decays exponentially in the frequency range of  $f \leq 80$  kHz showing several quasicohherent features in the frequency range of  $f < 20$  kHz.

Wave numbers of the fluctuations have been measured using two poloidally separated probes as  $k_\theta = \Delta\phi/\Delta y$ , where  $\Delta\phi$  is the phase shift and  $\Delta y$  is the poloidal separation between the probes. This has been analyzed in the frequency domain and the  $k_\theta(f)$  dependence is shown in Fig. 1(b) by the gray line. This dependence has a linear trend, however a large ripple is usually observed. This ripple can be reduced by statistical averaging over a large number of realizations. The origin of the large ripple in the  $k_\theta(f)$  dependence is currently under investigation. Preliminary results show that the amplitude of the ripple of the  $k_\theta(f)$  curve correlates with the relative strength of coherent structures to the level of broadband fluctuations. Zonal flows are commonly observed among the structures.<sup>25</sup> It has been shown recently<sup>13</sup> that in the presence of the zonal flow, phases of potential fluctuations become more random, which could therefore affect the  $k_\theta(f)$  measurements. The linear approximation of the dispersion is shown in Fig. 1(b) by the black line. The fluctuation phase velocity derived from this linear dispersion is within 10% of the measured  $\mathbf{E} \times \mathbf{B}$  drift velocity in this radial region.

### B. Justification of single-field model

The mode coupling mechanism in the turbulence may arise from the  $\mathbf{E} \times \mathbf{B}$  convection of the density fluctuations<sup>31</sup> or from the polarization drift<sup>20</sup> both of which appear in the equation of the ion dynamics:<sup>32</sup>

$$\partial n_i / \partial t + \mathbf{V}_E \cdot \nabla n_i + \nabla \cdot (n_i \mathbf{V}_p) = 0. \quad (1)$$

Here  $\mathbf{V}_E$  and  $\mathbf{V}_p$  are the fluctuating  $\mathbf{E} \times \mathbf{B}$  and the polarization drift velocities correspondingly and  $n_i = n_0 + \tilde{n}_i$  consists of mean and fluctuating parts. The  $\mathbf{E} \times \mathbf{B}$  nonlinearity arises from the  $\mathbf{V}_E \cdot \nabla \tilde{n}_i$  term while the polarization drift nonlinearity originates from the  $n_0 \nabla \cdot \mathbf{V}_p$  term.

The electron density fluctuations are considered as a sum of the adiabatic (Boltzmann) and nonadiabatic parts:  $\tilde{n}_e = n_0 \exp(e\tilde{\phi}/T) + \delta n_e$ . If  $\delta n_e = 0$  the problem can be reduced to a single-field model by substituting  $\tilde{n}_i = \tilde{n}_e$  in the Eq. (1) and rewriting it for the potential fluctuations  $\tilde{\phi}$ . In other words, when  $\delta n_e = 0$ ,  $\tilde{\phi}$  and  $\tilde{n}_e$  should be in phase. This would also mean no turbulent transport,  $\Gamma_{\text{turb}} = \langle \tilde{n}_e \tilde{E}_\theta / B_T \rangle = 0$  (brackets indicate time averaging), because  $\tilde{n}_e$  and the poloidal electric field fluctuations  $\tilde{E}_\theta$  would have a  $\pi/2$  phase shift ( $\tilde{E}_\theta = -\nabla_\theta \tilde{\phi}$ ). The adiabatic electron response should also indicate that the polarization drift dominates over the  $\mathbf{E} \times \mathbf{B}$  drift nonlinearity. It has been shown in Ref. 33, that the former dominates at large  $k_\perp \rho_s$  (where  $k_\perp$  is the perpendicular wave number and  $\rho_s$  is the ion gyroradius at the electron temperature), while the latter is dominant at small  $k_\perp \rho_s$ . The two nonlinearities are approximately equal when  $k_\perp \rho_s = \delta = c_s / (L_n \nu_e)$ . Here  $c_s$  is the ion acoustic velocity,  $L_n$  is the density scale length and  $\nu_e$  is the electron collision rate.

In our experiment  $k_\perp \rho_s (= 0.5 - 2.5) \gg \delta (\approx 0.1)$ , due to the large ion mass (argon), low magnetic field and high collisionality. Thus we expect the polarization drift to dominate over  $\mathbf{E} \times \mathbf{B}$  drift nonlinearity. This correlates with our measurements of the phase shift between  $\tilde{n}_e$  and  $\tilde{E}_\theta$  shown in Fig. 1(c). This phase shift is close to  $\pi/2$  over the entire spectrum suggesting the adiabatic electron response. We also find that the density and potential fluctuations are well correlated in the spectral range of interest. Figure 1(d) shows that the coherence between  $\tilde{n}_e$  and  $\tilde{\phi}$  is about 0.6 over a broad spectral range, also confirming our conclusion about adiabatic electron response.

To summarize, the above results and estimates justify that a single-field model<sup>19</sup> is used for the analysis of the spectral power transfer in the H-1 turbulence.

### C. Power transfer function estimation and amplitude correlation technique

For the sake of completeness we describe the analysis techniques proposed in Refs. 18 and 19. To estimate the nonlinear coupling coefficients and the energy transfer between waves for a fully turbulent system, it can be assumed that the nonlinear wave coupling equation can be written in the form<sup>19</sup>

$$\begin{aligned} \frac{\partial \phi(k, t)}{\partial t} = & (\gamma_k + i\omega_k) \phi(k, t) \\ & + \frac{1}{2} \sum_{\substack{k_1, k_2 \\ k = k_1 + k_2}} \Lambda_k^Q(k_1, k_2) \phi(k_1, t) \phi(k_2, t), \end{aligned} \quad (2)$$

where the spatial Fourier spectrum  $\phi(k, t)$  of the fluctuating field is defined by  $\varphi(x, t) = \sum_k \phi(k, t) e^{ikx}$ . The wave cou-

pling equation describes the rate of change of the spectrum due to linear and nonlinear (quadratic) effects, namely, due to the growth rate  $\gamma_k$ , the dispersion relation  $\omega_k$ , and the wave-wave coupling coefficient  $\Lambda_k^Q(k_1, k_2)$ . The coupling coefficient  $\Lambda_k^Q(k_1, k_2)$  describes the strength of the coupling which leads to a decay of the  $(k, \omega)$  wave into two waves  $(k_1, \omega_1)$  and  $(k_2, \omega_2)$ , or to the merging of two waves into one.

It is convenient to represent the spectrum  $\phi(k, t)$  by its amplitude and its phase, where the amplitude is slowly varying in time with respect to the phase changes as  $\phi(k, t) = |\phi(k, t)| e^{i\Theta(k, t)}$ .

The change of the spectrum in time, Eq. (2), can then be estimated by a difference approach:

$$\begin{aligned} \frac{\partial \phi(k, t)}{\partial t} = & \lim_{\tau \rightarrow 0} \left( \frac{|\phi(k, t + \tau)| - |\phi(k, t)|}{\tau} \frac{1}{|\phi(k, t)|} \right. \\ & \left. + i \frac{\Theta(k, t + \tau) - \Theta(k, t)}{\tau} \right) \phi(k, t). \end{aligned} \quad (3)$$

Substituting Eq. (2) into Eq. (3) and solving for  $\phi(k, t + \tau)$  with a very short time interval  $\tau$ , we obtain

$$\begin{aligned} \phi(k, t + \tau) = & \frac{\Lambda_k^L \tau + 1 - i[\Theta(k, t + \tau) - \Theta(k, t)]}{e^{-i[\Theta(k, t + \tau) - \Theta(k, t)]}} \phi(k, t) \\ & + \frac{1}{2} \sum_{\substack{k_1, k_2 \\ k = k_1 + k_2}} \frac{\Lambda_k^Q(k_1, k_2) \tau}{e^{-i[\Theta(k, t + \tau) - \Theta(k, t)]}} \\ & \times \phi(k_1, t) \phi(k_2, t), \end{aligned} \quad (4)$$

where  $\Lambda_k^L = \gamma_k + i\omega_k$ .

The spectrum at  $t + \tau$ ,  $\phi(k, t + \tau)$  is thus defined by the spectrum  $\phi(k, t)$  at  $t$  through the linear coefficient  $\Lambda_k^L$  and the quadratic coefficient  $\Lambda_k^Q(k_1, k_2)$ . To simplify, we redefine  $X_k = \phi(k, t)$ ,  $Y_k = \phi(k, t + \tau)$  and

$$L_k = \frac{\Lambda_k^L \tau + 1 - i[\Theta(k, t + \tau) - \Theta(k, t)]}{e^{-i[\Theta(k, t + \tau) - \Theta(k, t)]}}, \quad (5)$$

$$Q_k(k_1, k_2) = \frac{\Lambda_k^Q(k_1, k_2) \tau}{e^{-i[\Theta(k, t + \tau) - \Theta(k, t)]}}, \quad (6)$$

where  $k = k_1 + k_2$ . Then Eq. (4) can now be written as

$$Y_k = L_k X_k + \frac{1}{2} \sum_{\substack{k_1, k_2 \\ k = k_1 + k_2}} Q_k(k_1, k_2) X_{k_1} X_{k_2}. \quad (7)$$

The wave coupling equation (7) is thus represented by a model in which the output signal  $Y_k$  contains linear and nonlinear (quadratic) responses to the input signal  $X_k$ . The coefficients  $L_k$  and  $Q_k(k_1, k_2)$  are referred to as the linear transfer function and the quadratic transfer function, correspondingly.

The wave kinetic equation with the spectral power  $P_k = \phi(k, t) \phi_k^*(t)$  (asterisk denotes complex conjugate) can then be written as



$$\partial P_k / \partial t \approx \gamma_k P_k + \sum_{\substack{k_1, k_2 \\ k = k_1 + k_2}} T_k(k_1, k_2), \quad (8)$$

where  $T_k(k_1, k_2) = \text{Re}[\Lambda_k^Q(k_1, k_2) \langle \phi_k^* \phi_{k_1} \phi_{k_2} \rangle]$  is the nonlinear power transfer function, which quantifies the energy exchanged between different waves in the spectrum due to three-wave interactions.

The energy stored in the electrostatic fluctuations  $\phi_k$  can be written as<sup>15</sup>  $W_k = (1 + k_\perp^2) |\phi_k|^2$ . The nonlinear energy transfer function (NETF) then can be defined as

$$W_{\text{NL}}^k = (1 + k_\perp^2) \sum_{\substack{k_1, k_2 \\ k = k_1 + k_2}} T_k(k_1, k_2). \quad (9)$$

To determine the coupling coefficients  $L_k$  and  $Q_k^{k_1, k_2}$  in Eq. (7), the linear growth rate  $\gamma_k$  and the  $T_k(k_1, k_2)$  of Eq. (8) and eventually  $W_{\text{NL}}^k$ , the following are needed: statistically averaged estimations of the auto-power spectrum  $\langle X_k X_k^* \rangle$ , cross-power spectrum  $\langle Y_k X_k^* \rangle$ , auto-bispectrum  $\langle X_k X_{k_1}^* X_{k_2}^* \rangle$ , cross-bispectrum  $\langle Y_k X_{k_1}^* X_{k_2}^* \rangle$  and the fourth order moment  $\langle X_{k_1} X_{k_2} X_{k_1'}^* X_{k_2'}^* \rangle$ .

In the process of estimation, the analyzed signal is divided into a large number of time segments (realizations),  $N_R$ , overlapping by 50%. Power spectra, bispectra and the fourth order moments are estimated for each realization. Then they are averaged over all realizations to compute the NETF. A proper choice of  $N_R$  will be discussed later.

To test the accuracy of the NETF estimation, we first generate some model data with known linear and nonlinear coupling coefficients as suggested in Ref. 19. The nonlinear coupling coefficients are chosen arbitrarily but have the same order of magnitude as the ones predicted by the Hasegawa–Mima equation. The linear coupling coefficient is defined such that the input and output spectra are similar as would be expected for a stationary state. Model tests have been performed as follows. The random noise signal is generated. The NETF estimation of this signal is performed to make sure that the nonlinear energy transfer is zero. Then the coupling coefficients are applied to the noise signal. This procedure is repeated several times to make sure that the resulting signal is non-Gaussian, i.e., that it has a non-zero bispectrum.

In Ref. 18 the fourth-order moment  $\langle X_{k_1} X_{k_2} X_{k_1'}^* X_{k_2'}^* \rangle$  is approximated by the square of the second-order moment  $\langle |X_{k_1} X_{k_2}|^2 \rangle$  by neglecting terms with  $(k_1', k_2') \neq (k_1, k_2)$ . This approximation is often used in weak turbulence theories and has also been applied to strong turbulence.<sup>19</sup> In the later modification of this method,<sup>21</sup> several improvements to the spectral power transfer estimation technique have been implemented. First, stationarity or statistical ergodicity of the turbulence is enforced to eliminate effects of noise and fluctuations not described by Eq. (7), which otherwise may, in principle, give unphysically large damping rates in the original method. Second, the fourth-order moment is retained. Both techniques have been tested using the simulated data.

Figure 2(a) shows spectra of the real part of the linear

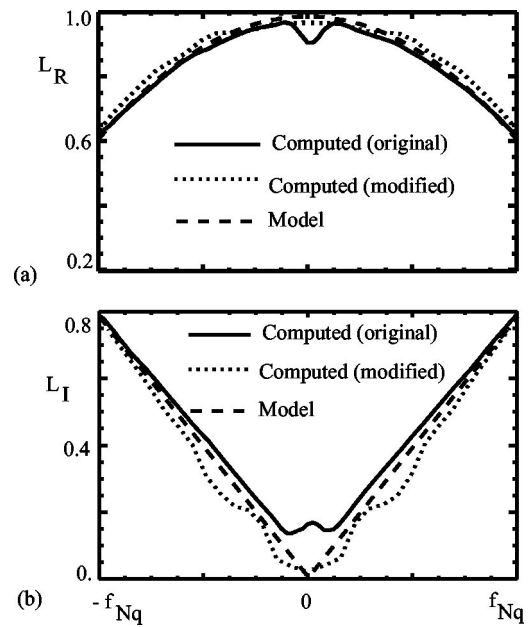


FIG. 2. (a) The real part  $L_R$  and (b) the imaginary part  $L_I$  of the linear coupling coefficient with model (dashed line), computed results using the original (Ref. 18) (solid line) and modified (Ref. 21) (dotted line) methods.  $f_{\text{Nq}}$  is the Nyquist frequency.

transfer function,  $L_R$  [see Eq. (7)], where the model and computed spectra using the original<sup>18</sup> and modified<sup>21</sup> methods are shown in dashed, solid, and dotted lines, respectively. Figure 2(b) shows the spectra of the imaginary part of the linear transfer function,  $L_I$ . These results indicate that both methods recover the transfer function  $L_k$  [Eq. (7)] almost equally well. Due to the stationarity approximation used in this nonlinear energy transfer model, the linear coupling is balanced by the nonlinear coupling between the modes. This is why only linear coefficients are shown in Fig. 2. Note that these results are obtained using 400 realizations so that each segment consists of 80 data points.

For the experimental data, the NETF are estimated using the original<sup>18</sup> and the modified<sup>21</sup> methods. Both results are in the qualitative agreement. All experimental results presented in this paper are obtained by retaining the fourth-order moments in the computation of NETF.

Averaging over a large number of realizations is essential for the statistical error of the higher-order spectral estimation to be small. We introduce two parameters which characterize the numerical convergence of the method. The first one is the total positive value of the power transfer estimation,  $P_{\text{tot}} = \sum_k (T_k(k_1, k_2) > 0)$ . The second parameter is the maximum value of the estimated linear growth rate,  $\gamma_{\text{max}} = \max(\gamma_k)$  with  $\gamma_k$  defined as in Eq. (8). Figure 3(a) shows these two parameters as functions of the number of realizations,  $N_R$ .  $P_{\text{tot}}$  decreases rapidly with the increase in  $N_R$  when  $N_R$  is less than 200. Stable  $P_{\text{tot}}$  is obtained when  $N_R$  reaches 400. It can be seen that stable  $\gamma_{\text{max}}$  computation can be obtained when  $N_R$  exceeds 430.

It is also important to estimate the accuracy of the results using some physically meaningful criterion. The energy conservation in the spectrum,  $\sum_k W_{\text{NL}}^k = 0$ , is used as the “test of

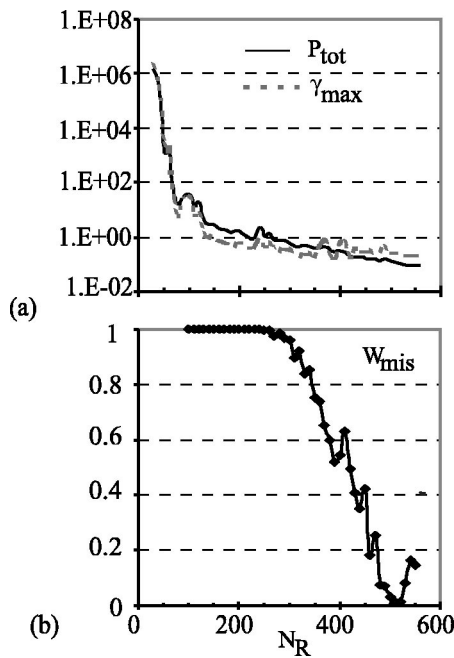


FIG. 3. (a)  $P_{tot}$  (solid line) and  $\gamma_{max}$  (dashed line) and (b)  $W_{mis}$  of the power transfer function estimation as a function of the number of realizations,  $N_R$ .

goodness" of the estimation. We define the error in the energy conservation as  $W_{mis} = \sum_k W_{NL}^k / \sum_k |W_{NL}^k|$ . Thus,  $W_{mis}$  characterizes the energy mismatch. When the energy conservation is satisfied, that is when  $\sum_k W_{NL}^k = 0$ ,  $W_{mis} = 0$ . In Fig. 3(b) we show  $W_{mis}$  as a function of  $N_R$ . At small numbers of realizations, the result is meaningless since computations have not converged, as seen in Fig. 3(a). When  $N_R$  is between 450 to 550,  $W_{mis}$  decreases to less than 20%.  $W_{mis}$  increases again after  $N_R$  exceeds 550. This increase is probably due to the fact that the frequency resolution of the estimation becomes too poor at large  $N_R$  if the signal length is fixed. The number of realizations is chosen by trading off minimal  $W_{mis}$  for a slightly better frequency resolution at  $N_R = 460$ .

In the model described by Eq. (8), the wave number domain is transformed into the frequency domain, so that the three-wave interactions satisfying matching conditions  $k = k_1 + k_2$  obey the frequency selection rule,  $f = f_1 + f_2$ . This transformation is justified in case of the linear dispersion. In our conditions, such a dispersion is confirmed by the linear trend of the measured  $k_\theta(f)$  spectrum shown in Fig. 1(b).

A floating potential signal is digitized at 0.3 MHz while the typical plasma pulse length is  $\sim (60-80)$  ms. The signal is divided into 460 overlapping segments, so that each segment contains 80 data points. Such a severe statistical averaging results in the reduced frequency resolution of the spectra of the NETF,  $\Delta f \approx 4$  kHz. Considering the large amount of averaging needed to obtain the linear  $k_\theta(f)$  dependence, we may suggest that the averaging needed for the NETF estimation is not just a numerical effect, but it is dictated by the need to satisfy the model assumption about the  $k_\theta(f)$  linearity.

The amplitude correlation is another technique which has been used in studies of nonlinear energy transfer in the

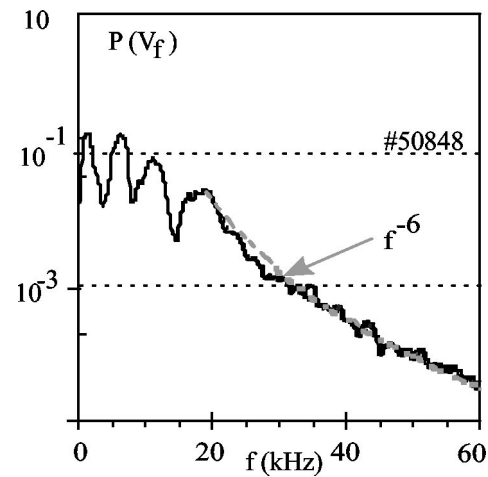


FIG. 4. Power spectrum of the floating potential fluctuations.

fluctuation spectrum.<sup>23</sup> Two frequency bands of interest are selected from the fluctuation signal, which are first bandpass filtered to obtain two time series. These two time series are then squared and passed through a low-pass filter to obtain only the slow varying amplitude information. Then the cross-correlation function (CCF) between these signals is computed,  $K(\tau) = \langle [x_1^2(t)][x_2^2(t+\tau)] \rangle$ . The energy flow direction can then be determined from the sign of the time delay of the CCF.

### III. RESULTS ON THE SPECTRAL ENERGY TRANSFER ANALYSIS

A typical power spectrum of the floating potential fluctuations in the L-mode plasma discharge in H-1 is shown in Fig. 4. The spectrum contains several coherent features in the frequency range of  $f \leq 20$  kHz and an exponentially decaying broadband turbulence up to the frequency of  $f \approx 80$  kHz.

The NETF, the linear growth rate  $\gamma_k$  derived from Eq. (8) and the power spectrum are shown in Fig. 5. The frequency resolution here is  $\Delta f \approx 4$  kHz. As a result of this low frequency resolution, coherent spectral features seen in Fig. 4 do not show up in Fig. 5(a). The nonlinear energy transfer function  $W_{NL}^k$  is presented in Fig. 5(b).  $W_{NL}^k$  is negative in the broadband spectral region of  $f = (20-50)$  kHz suggesting that waves in this range lose energy, whereas the lower frequency spectral components ( $f < 20$  kHz) gain energy. It is in this spectral region where strong quasicohherent fluctuations in L-mode are observed as seen in Fig. 4. It is natural to suggest that these structures are generated nonlinearly as a result of the inverse energy cascade in the spectrum. The linear growth rate shown in Fig. 5(c) has maximum at  $f \approx 25$  kHz. This range is identified as the unstable range, as will be discussed later.

The inverse energy cascade similar to that shown in Fig. 5 is observed in all plasma discharges in which strong coherent structures are generated. It has been shown in Ref. 36 that the coherent fluctuations in H-1 observed using both 2D-scannable probe and the two-view multi-channel spectroscopy diagnostic are the dipole structures propagating in

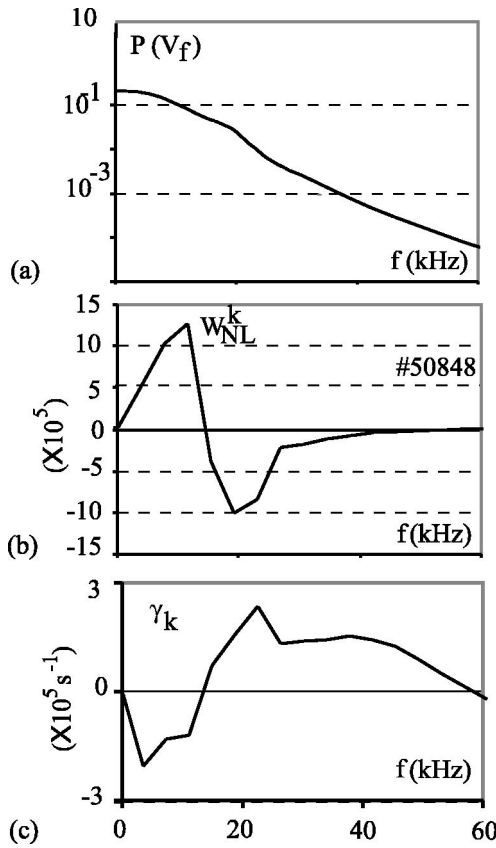


FIG. 5. (a) Power spectrum of the floating potential fluctuations; (b) the nonlinear energy transfer function  $W_{NL}^k$ ; (c) linear growth rate  $\gamma_k$  derived from Eq. (8). The frequency resolution is  $\Delta f \approx 4$  kHz.

the poloidal direction. Another example of turbulent structures observed in H-1 are zonal flows found in the L-mode.<sup>25</sup> We will discuss zonal flows later in this paper.

As seen in Fig. 4, the L-mode spectrum obeys the power law fit of  $P(\phi\phi^*) \sim f^{-\alpha}$ , where  $\alpha \approx 6$ . This power law holds over 3 decades in the L-mode spectrum and is observed in all spectra in which the low frequency condensate is present. Since for large wave numbers the spectral energy is  $W_k \sim k^2 P_k$ ,<sup>15</sup> the observed scaling  $W \sim k^{-4}$  agrees with the theoretically expected scalings of  $W \sim k^{-4}$  (Ref. 15) and  $P(\phi\phi^*) \sim k^{-6}$ .<sup>35</sup>

The above results on the nonlinear energy transfer function indicate that the spectral energy is transferred from a higher frequency range to a low frequency range where coherent structures are observed. However, in view of the poor spectral resolution, it is not clear if the spectral energy flows from the higher frequency range predominantly to the coherent modes, or if it is distributed evenly into the broadband turbulence. The amplitude correlation technique is used here to study the energy flow with a better frequency resolution.

Shown in Fig. 6(a) is the power spectrum of the floating potential fluctuations. The shaded spectral region of (0–15) kHz corresponds to the region which nonlinearly receives spectral energy, as observed in Fig. 5(b). The second shaded spectral region of (20–50) kHz corresponds to the region giving the energy away. The CCF between these two frequency bands is shown in Fig. 6(b). The maximum correla-

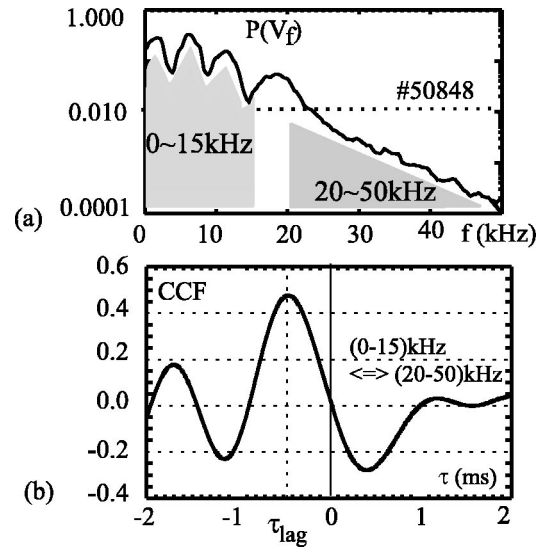


FIG. 6. (a) The power spectrum of the fluctuation showing two frequency ranges for the amplitude correlation (shadowed); (b) the amplitude correlation between the frequency bands of (0–15) kHz and (20–50) kHz in the L mode.

tion is high,  $\max(\text{CCF}) \approx 0.5$ . The CCF has a maximum at the negative time lag which means that the amplitude of the low frequency band lags with respect to the higher frequency band. The interpretation of the negative time lag is that the low frequency band receives its energy from the higher frequency band.<sup>23</sup> This result agrees with the NETF estimation result which also suggests the higher frequency band being the donor of the spectral energy and the low frequency being the receiver.

Now we ask a more specific question: where does the nonlinear energy flow in the low frequency band? The amplitude correlation functions between frequency bands of  $f \approx 6.7$  kHz and  $f \approx 23$  kHz, and of  $f \approx 8$  kHz and  $f \approx 23$  kHz are shown in Fig. 7. Frequencies  $f \approx 6.7$  kHz and  $f \approx 8$  kHz are chosen from the power spectrum of Fig. 7(a), such that the  $f \approx 6.7$  kHz corresponds to a maximum of one of the structures while the  $f \approx 8$  kHz corresponds to a local minimum in the spectrum. The frequency of  $f \approx 23$  kHz is chosen to represent the frequency band of the source. It is at this frequency where the linear growth rate has maximum as seen in Fig. 5(c). The width of the frequency band for the CCF computations is chosen as  $\Delta f = 1$  kHz. The CCF between the frequency bands of  $f \approx 6.7$  kHz and  $f \approx 23$  kHz is shown in Fig. 7(b). The negative time lag indicates that the  $f \approx 6.7$  kHz feature receives energy from the  $f \approx 23$  kHz band. The maximum of the correlation function is high,  $\max(\text{CCF}) \approx 0.5$ . The CCF between the frequency bands of  $f \approx 8$  kHz and  $f \approx 23$  kHz is shown in Fig. 7(c). The CCF is lower compared with Fig. 7(b). This low correlation between the source and the local minimum is probably due to a lower nonlinear coupling between these two bands.

The above results indicate that the spectral energy is mostly delivered into coherent structures. We observe high levels of the correlation between selected frequency bands in the unstable spectral region of (20–40) kHz and the frequencies of the coherent structures. This is illustrated in Fig. 8(a)

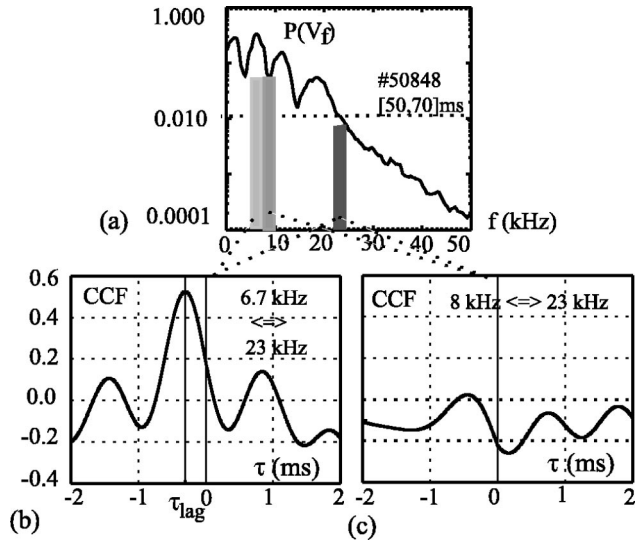


FIG. 7. (a) The power spectrum of the floating potential fluctuation. Shaded bands correspond to the frequency ranges used in the CCF estimation; CCF (b) between  $f \approx 6.7$  kHz and  $f \approx 23$  kHz, and (c) between  $f \approx 8$  kHz and  $f \approx 23$  kHz.

in which maxima of the CCF between  $f_1 = 6.7$  kHz and  $f_s$  in the range from 20 to 40 kHz are plotted against frequency  $f_s$ . Several prominent peaks in this plot correspond to frequencies satisfying the matching rule  $f_1 = f_3 - f_2$  for the three-wave interactions involving  $f_1 = 6.7$  kHz. High values of the maxima of the CCF point to the conclusion that the inverse energy cascade which leads to the generation of the coherent structures is due to the *coherent phase* three-wave interactions. Figure 8(b) shows similarly computed CCF maxima for the frequency band of a local minimum in the

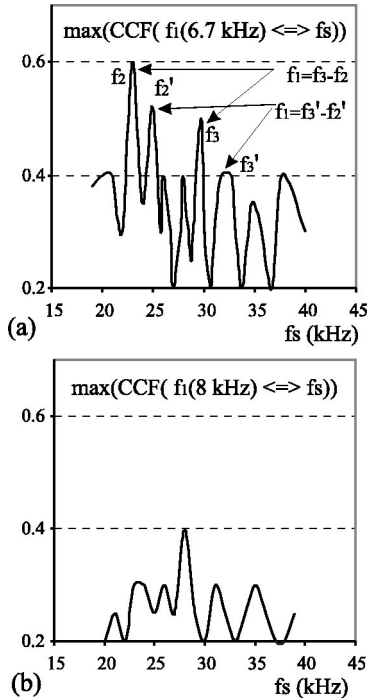


FIG. 8. The maximum of the CCF between  $f_1$  and  $f_s$ , with (a)  $f_1 = 6.7$  kHz; (b)  $f_1 = 8$  kHz, respectively.  $f_s$  varies between 20–40 kHz.

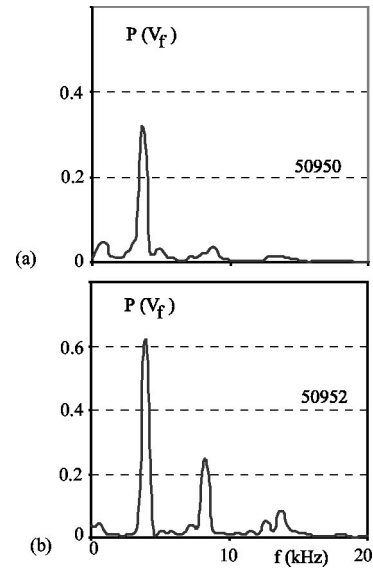


FIG. 9. Power spectra of the floating potential fluctuations at (a)  $B = 0.05$  T; (b)  $B = 0.062$  T, respectively.

spectrum at  $f_1 = 8$  kHz. The maxima do not exceed 0.4 anywhere in the spectral range of (20–40) kHz. Thus we may speculate that the broadband part of the low frequency range is driven mostly by the *random phase* three-wave interactions.

We can summarize at this point that the low-frequency coherent structures, or the condensate<sup>15</sup> are driven via the inverse energy cascade from the unstable range. Now we will discuss the spectral content of the condensate and its relation to the nonlinear energy transfer.

Fluctuation spectra in the L-mode of confinement in H-1 depend on the magnetic field and on the RF power. Both  $B$  and  $P_{rf}$  can be used as control parameters to drive plasma to the confinement bifurcation.<sup>37</sup> As the magnetic field is increased, an increase in the number of spectral features in the condensate is observed. At higher  $B$ , closer to the L-H bifurcation, zonal flows appear in the condensate spectra.<sup>30</sup> Changes in the spectra with  $B$  are illustrated in Fig. 9 for two magnetic fields,  $B = 0.05$  T and  $B = 0.062$  T. The increase in the number of spectral features as well as in the spectral power of the fluctuations is evident from Fig. 9.

The increase in the spectral power of the condensate with  $B$  is correlated with an increase in the pressure gradient in the plasma during the  $B$ -scan. The pressure gradient is believed to be the free energy reservoir for the underlying linear instability.<sup>30</sup> We estimate the pressure gradient  $\nabla P_i$  from the radial force balance equation

$$E_r \approx (Z_i e n_i)^{-1} \nabla P_i, \quad (10)$$

in which the ion velocity terms  $v_{\theta i} B_\phi$  and  $v_{\phi i} B_\theta$  are neglected for the reasons discussed in Ref. 34.

The ion pressure gradient is estimated from the measured radial electric field,  $E_r$ , and the electron density,  $n_e$ , as  $\nabla P_i = (Z_i e n_i) E_r$ . The estimated ion pressure gradient increases with  $B$ . Figure 10 shows the linear growth rate  $\gamma_k$  averaged over the range of  $f = (25-35)$  kHz versus the estimated ion pressure gradient. The instability growth rate ap-



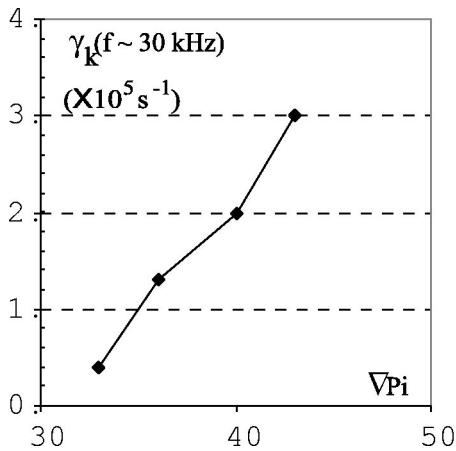


FIG. 10. The computed linear growth rate  $\gamma_k$  around 30 kHz versus the estimated  $\nabla P_i$ .

pears to be well correlated with the free energy level as measured by  $\nabla P$ , thus confirming that the resistive pressure-gradient-driven mode is the likely candidate for the fluctuations in H-1.<sup>30</sup> As the free energy driving the instability increases, the linear growth rate is also increased. As the result, the total nonlinear energy outflow from the unstable range increases leading to a larger spectral energy transfer into the coherent structures. The spectral power of the condensate is also increased.

The above conclusions are also confirmed by comparing spectra and spectral transfer functions across the confinement transitions in H-1. Two plasma confinement modes, namely, L and H modes, are observed in the H-1 heliac at low magnetic fields ( $B \leq 0.2$  T).<sup>30</sup> Close to the L–H transition threshold plasma spontaneously jumps from L to H mode within  $\sim 1$  ms. The electron density and the ion temperature of the plasma increase across the transition by (50–100)%. Transitions are accompanied by the fluctuation suppression and by the onset of the strongly sheared radial electric field,  $E_r$ .<sup>30</sup> Turbulence spectrum is strongly altered across the transition as shown in Fig. 11. The long wavelength fluctuations are suppressed in H-mode by the  $E_r$  shear as discussed in Ref.

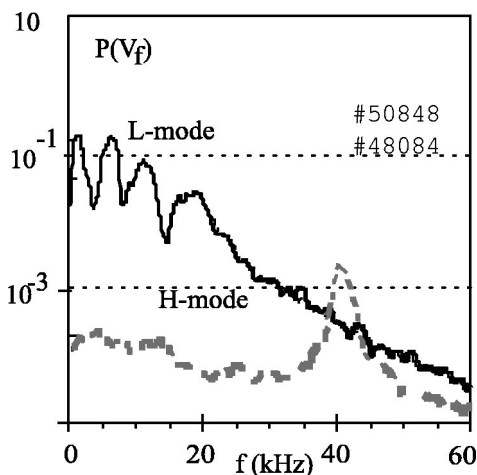


FIG. 11. Power spectra of the floating potential fluctuation in L (solid line) and H (dashed line) mode.

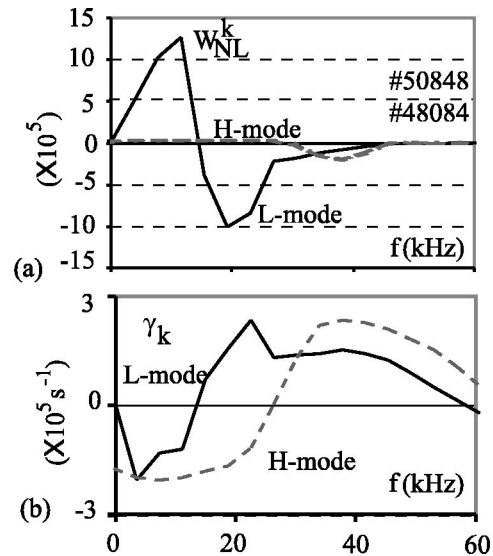


FIG. 12. (a) Nonlinear energy transfer function  $W_{NL}^k$ ; (b) linear growth rate  $\gamma_k$  in L (solid line) and H (dashed line) modes, respectively.

30. The fluctuation level is reduced across the L–H transition over the entire spectrum except for the region around  $f \approx 40$  kHz, where the fluctuation level even increases in H-mode. The convergence test of the NETF calculation is performed for H-mode data and we find that the convergence is faster in H-mode compared with L-mode, probably due to a narrower fluctuation spectrum (just one peak at 40 kHz seen in Fig. 11).

Figure 12 shows the NETF,  $W_{NL}^k$  and linear growth rates  $\gamma_k$  computed for the fluctuations in the floating potential in L and H confinement modes. The linear growth rate  $\gamma_k$  is shown in Fig. 12(b). This growth rate has a positive maximum at  $f \approx 25$  kHz in L-mode, while in H-mode it peaks at  $f \approx 40$  kHz. The frequency shift of the maximum of the linear growth rate from 25 kHz in L-mode to 40 kHz in H-mode is probably due to an increase in the radial electric field and the associated Doppler shift across the L–H transition.<sup>34</sup>

The  $f \approx 40$  kHz feature in the H-mode spectrum seen in Fig. 11 is probably indicative of the spectral region of the underlying linear instability which also drives turbulence in the L-mode. We may speculate that when the nonlinear spectral transfer is high in the L-mode, the energy is transferred from the initially unstable region of  $f \approx 25$  kHz both up and down the spectrum, with the inverse cascade dominating over the forward cascade. The inverse cascade leads to the formation of the spectral condensate observed as quasicohherent structures. When the level of  $W_{NL}^k$  around  $f \approx 40$  kHz is reduced in H-mode as seen in Fig. 12(a), the spectral energy becomes peaked in this spectral region. Since the free energy for this instability (pressure gradient) is increased across the transition from L to H mode (more peaked density profile in H-mode<sup>30</sup>), one would expect a linear growth rate to increase. This expectation agrees with the observed increase in the fluctuation level at  $f \approx 40$  kHz seen in Fig. 11 and also with our estimation of the linear growth rate shown in Fig. 12(b).



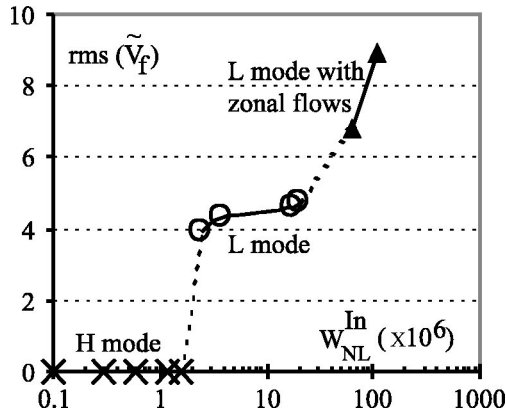


FIG. 13. Root-mean-square value of  $\tilde{V}_f$  (proportional to the spectral power of the condensate) as a function of the nonlinear energy transfer  $W_{NL}^{In}$  into the spectral range of  $f \leq 20$  in L (circles and triangles) and H (crosses) modes.

The condensate formation is linked to the level of the energy which is nonlinearly transferred into the low frequency part of the spectrum. A correlation between the inverse cascade of energy from the unstable range and the spectral power in the low-frequency range is illustrated in Fig. 13 which combines results of the spectral energy transfer estimation in L and H modes during the *B*-scan.  $W_{NL}^{In}$  is defined as the total nonlinear energy flow into the low frequency range,  $W_{NL}^{In} = \sum_k (W_{NL}^k > 0)$ . The spectral power in the range of  $f \leq 20$  kHz increases with  $W_{NL}^{In}$  in this range in L-mode, while in H-mode a zero spectral power (no condensate in H-mode) is observed at nonzero spectral energy transfer,  $0.1 < W_{NL}^{In} \times 10^{-6} < 3$ . Such a dependence may be indicative of the threshold nature of the condensate generation via the inverse energy cascade.

It has been mentioned earlier that when the nonlinear energy transfer becomes sufficiently high, we observe zonal flows, which typically appear as one of the coherent features in the condensate spectrum. Zonal flows are poloidally symmetric ( $k_r \gg k_\theta \sim 0$ , where  $k_r$  and  $k_\theta$  are the radial and poloidal wave number, respectively) potential structures observed in the L-mode discharges in H-1.<sup>25</sup> Figure 14(a) shows an example of such a spectrum containing a zonal flow feature at  $f = 6$  kHz. The nonlinear energy transfer function is shown in Fig. 14(b). This NETF is qualitatively similar to the NETF of other spectra containing coherent structures. Similarly to other coherent structures, the energy is transferred directly from the unstable region into zonal flows. This is illustrated in Fig. 14(c) which shows the CCF between the frequency band of the zonal flow  $f \sim 6$  kHz ( $\Delta f = 1$  kHz) and the unstable range of  $f = 18$ –24 kHz. The maximum correlation is high,  $\max(\text{CCF}) \approx 0.6$ . As in cases with other coherent structures, the CCF between the zonal flow and the unstable range has maximum at the negative time lag, confirming the energy transfer from higher to lower frequencies.

Zonal flows are typically localized in the plasma in a relatively narrow radial region, as described in Ref. 13. A radial profile of the normalized intensity of the zonal flow defined as  $\tilde{E}_r(6 \text{ kHz}) / \langle E_r \rangle$  (Ref. 13) is shown in Fig. 15(a). The zonal flow has a maximum at the radial position of  $\rho$

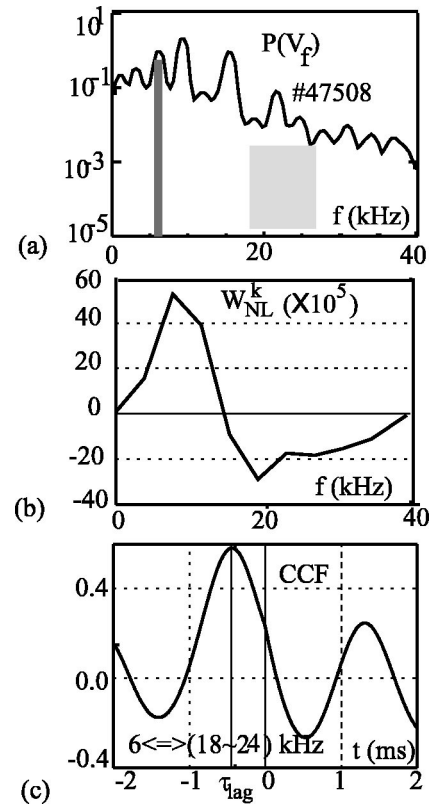


FIG. 14. (a) Power spectrum of the floating potential fluctuations. A  $f = 6$  kHz feature has been identified as a zonal flow. (b) The nonlinear energy transfer function. (c) The cross-correlation function between the zonal flow frequency band and the unstable range of  $f = 18$ –24 kHz.

$\approx 0.4$  and its minimum is at  $\rho \approx 0.7$ . The root-mean-square level of the poloidal electric field fluctuations  $\tilde{E}_\theta$ , is also shown in Fig. 15(a). The  $E_\theta$  fluctuation level does not change very much along the radius. A total nonlinear energy

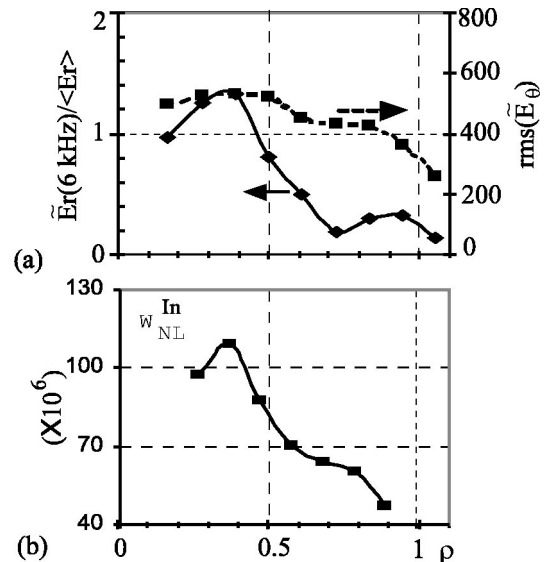


FIG. 15. Radial profile of (a) the normalized fluctuations in the radial electric field due to the zonal flow like structure at  $f = 6$  kHz (solid line) and the fluctuation amplitude in the poloidal electric field (dashed line); (b) the total nonlinear energy flows into the low frequency range of the spectrum,  $W_{NL}^{In}$ .

flow into the low frequency range,  $W_{NL}^{In}$ , is plotted in Fig. 15(b) as a function of the radial position. The maximum nonlinear energy flow  $W_{NL}^{In}$  is observed at  $\rho=0.4$ , which corresponds to the maximum level of the zonal flow shown in Fig. 15(a). The profile of  $W_{NL}^{In}$  is similar to the profile of the zonal flow level.

#### IV. CONCLUSIONS

Detailed studies of the spectral transfer in turbulent spectra in the H-1 heliac have been performed. Main issues addressed in this paper are related to mechanisms of generation of large coherent structures and zonal flows.

Two methods of analysis were used in these studies: the nonlinear power transfer function estimation method<sup>18,21</sup> and the amplitude correlation technique.<sup>23</sup> It has been demonstrated that these methods complement each other. The PTF method gives good estimation of the average energy transfer within spectra, while the CCF computations allow a better spectral resolution to be achieved. Both methods rely on a single-field description of the plasma turbulence. It is demonstrated that such an approximation is justified in the reported experiments. In the H-1 plasma the polarization drift nonlinearity dominates over the  $\mathbf{E} \times \mathbf{B}$  drift nonlinearity due to the large ion gyroradius and high collisionality thus making the Hasegawa–Mima model of turbulence<sup>20</sup> a good approximation in our conditions.

It has been shown that the frequency spectra of the fluctuations in the electrostatic potential exhibit exponentially decaying broadband fluctuations (0–80 kHz) and strong coherent structures in the lower frequency range (0–20 kHz). The inverse energy cascade from the spectral region of the underlying linear instability (20–30 kHz) to the low frequency range is observed in all L-mode spectra. The unstable range has been identified as a region of the largest positive linear growth rate. The growth rate increases with the increase of the plasma pressure gradient which is believed to be the free energy source for linear instability.

Coherent structures which exist in the low frequency range receive their energy nonlinearly from the unstable range. Results obtained using the amplitude correlation technique indicate that the spectral energy flows from the source, directly into coherent structures. Large amplitudes of the cross-correlation functions are indicative of the coherent phase three-wave interactions between structures and the unstable range.

A very similar situation is observed for zonal flows. Strong inverse energy cascades are observed when zonal flows are generated in the plasma. Radial regions of the strongest zonal flow and that of the largest (positive) nonlinear energy transfer function coincide, as seen in Fig. 15.

The spectral power of the condensate is found to correlate with the nonlinear energy transfer into the low frequency range,  $W_{NL}^{In}$ . Above a certain threshold value of  $W_{NL}^{In}$  coherent structures are formed. Below this threshold, presumably only the broadband turbulence is developed. Further increase in  $W_{NL}^{In}$  leads to the generation of zonal flows as seen in Fig. 13. Shown in this figure is the root-mean-square value of the

$\tilde{V}_f$  fluctuations, which is proportional to  $W_{NL}^{In}$  (since coherent structures dominate the spectrum, see Fig. 9).

The analysis of the spectrum evolution across L–H transitions shows that the linear growth rate of the instability increases from L to H-mode of confinement. Both inverse and forward energy cascades are substantially reduced from L to H mode as seen in Fig. 12. The most significant difference between the two modes is the onset of the strongly sheared radial electric field in H-mode. One could speculate that the decorrelation of the large structures by this sheared  $E_r$  is responsible for the dramatic decrease in the spectral power in the low-frequency part of the spectrum. It is not clear however, why forward cascade from the unstable range toward smaller scale fluctuations is reduced. Such a reduction is evident from the decreased fluctuation level in the frequency range from 45 to 60 kHz seen in Fig. 11. One can assume that in H-mode the spectral energy from the unstable range is transferred into the  $f=0$  zonal flow, pumping the spectral energy directly into the mean sheared  $E_r$ .

#### ACKNOWLEDGMENTS

The authors would like to thank W. M. Solomon for useful discussions and K. Shats for careful reading of the manuscript.

- <sup>1</sup>W. Horton and Y.H. Ychikawa, *Chaos and Structures in Nonlinear Plasmas* (World Scientific, Singapore, 1996).
- <sup>2</sup>A. Okamoto, K. Hara, K. Nagaoka, S. Yoshimura, J. Vranjes, M. Kono, and M.Y. Tanaka, *Phys. Plasmas* **10**, 2211 (2003).
- <sup>3</sup>M.Y. Tanaka and M. Kono, *J. Plasma Fusion Res.* **4**, 131 (2001).
- <sup>4</sup>T. Huld, A.H. Mielsen, H.L. Pecseli, and J.J. Rasmussen, *Phys. Fluids B* **3**, 1609 (1991).
- <sup>5</sup>O. Grulke and T. Klinger, *New J. Phys.* **4**, 67.1 (2002).
- <sup>6</sup>J. Bleuel, M. Endler, H. Niedermeyer, M. Schubert, H. Thomsen, and the W7-AS team, *New J. Phys.* **4**, 38.1 (2002).
- <sup>7</sup>X.N. Su, W. Horton, and P.J. Morrison, *Phys. Fluids B* **3**, 921 (1991).
- <sup>8</sup>T. Tajima, W. Horton, P.J. Morrison, J. Schutkeker, T. Kamimura, K. Mima, and Y. Abe, *Phys. Fluids B* **3**, 938 (1991).
- <sup>9</sup>W. Horton and A. Hasegawa, *Chaos* **4**, 227 (1994).
- <sup>10</sup>P.H. Diamond, M.N. Rosenbluth, F.L. Hinton, M. Malkov, J. Fleischer, and A. Smolyakov, in *Plasma Physics and Controlled Nuclear Fusion Research*, 18th IAEA Fusion Energy Conference, Yokohama, Japan, 1998 (International Atomic Energy Agency, Vienna, 1998), p. IAEA-CN-69/TH3/1.
- <sup>11</sup>P. Terry, *Rev. Mod. Phys.* **72**, 109 (2000).
- <sup>12</sup>Z. Lin, T.S. Hamm, W.W. Lee, W.M. Tang, and R.B. White, *Science* **281**, 1835 (1998).
- <sup>13</sup>M.G. Shats, W.M. Solomon, and H. Xia, *Phys. Rev. Lett.* **90**, 125002 (2003).
- <sup>14</sup>R.H. Kraichnan, *Phys. Fluids* **10**, 1417 (1967).
- <sup>15</sup>A. Hasegawa, C.G. MacLennan, and Y. Kodama, *Phys. Fluids* **22**, 2122 (1979).
- <sup>16</sup>A. Hasegawa and M. Wakatani, *Phys. Rev. Lett.* **59**, 1581 (1987).
- <sup>17</sup>Y.C. Kim and E.J. Powers, *IEEE Trans. Plasma Sci.* **PS-7**, 120 (1979).
- <sup>18</sup>Ch.P. Ritz and E.J. Powers, *Physica D* **20**, 320 (1986).
- <sup>19</sup>Ch.P. Ritz, E.J. Powers, and R.D. Bengtson, *Phys. Fluids B* **1**, 153 (1989).
- <sup>20</sup>A. Hasegawa and K. Mima, *Phys. Fluids* **21**, 87 (1978).
- <sup>21</sup>J.S. Kim, R.D. Durst, R.J. Fonck, E. Fernandez, A. Ware, and P.W. Terry, *Phys. Plasmas* **3**, 3998 (1996).
- <sup>22</sup>J.S. Kim, R.J. Fonck, R.D. Durst, E. Fernandez, P.W. Terry, S.F. Paul, and M.C. Zarnstorff, *Phys. Rev. Lett.* **79**, 841 (1997).
- <sup>23</sup>F.J. Crossley, P. Uddholm, P. Duncan, M. Khalid, and M.G. Rusbridge, *Plasma Phys. Controlled Fusion* **34**, 235 (1992).
- <sup>24</sup>H.L. Pecseli and J. Trulsen, *Plasma Phys. Controlled Fusion* **35**, 1701 (1993).

- <sup>25</sup>M.G. Shats and W.M. Solomon, Phys. Rev. Lett. **88**, 045001 (2002).
- <sup>26</sup>M. Jakubowski, R.J. Fonck, and G.R. McKee, Phys. Rev. Lett. **89**, 265003 (2002).
- <sup>27</sup>H. Xia and M.G. Shats, Phys. Rev. Lett. **91**, 155001 (2003).
- <sup>28</sup>S.M. Hamberger, B.D. Blackwell, L.E. Sharp, and D.B. Shenton, Fusion Technol. **17**, 123 (1990).
- <sup>29</sup>M.G. Shats and W.M. Solomon, New J. Phys. **4**, 30 (2002).
- <sup>30</sup>M.G. Shats, Plasma Phys. Controlled Fusion **41**, 1357 (1999).
- <sup>31</sup>W. Horton, Phys. Rev. Lett. **37**, 1269 (1976).
- <sup>32</sup>P. Terry and W. Horton, Phys. Fluids **25**, 491 (1982).
- <sup>33</sup>D.E. Newman, P.W. Terry, P.H. Diamond, and Y.M. Liang, Phys. Fluids B **5**, 1140 (1993).
- <sup>34</sup>M.G. Shats, D.L. Rudakov, R.W. Boswell, and G.G. Borg, Phys. Plasmas **4**, 3629 (1997).
- <sup>35</sup>D. Fyfe and D. Montgomery, Phys. Fluids **22**, 246 (1979).
- <sup>36</sup>M.G. Shats and J. Howard, Fusion Eng. Des. **34–35**, 271 (1997).
- <sup>37</sup>M.G. Shats, C.A. Michael, D.L. Rudakov, and B.D. Blackwell, Phys. Plasmas **5**, 2390 (1998).